SDA Environment Toolkit for Defense (SET4D) – Enabling Attribution for Orbital Assets and Electro-magnetic Spectrum Links Through Streamlined R2O

Sage K. Andorka
Space Systems Command, Special Programs Directorate (SSC/ECZG)

Jeffery M. Cox
The Aerospace Corporation

Michael F. Fraizer
Space Systems Command, Special Programs Directorate (SSC/ECZG)

ABSTRACT

This paper describes the Space Domain Awareness (SDA) Environmental Toolkit for Defense (SET4D) migration and modernization of DoD space environment data and modeling capabilities to a GovCloud architecture and attribution tools for satellite anomalies, electro-magnetic interference (EMI) and launch and predict impact (L&PI) assessments. During the cloud migration, SMC/SPG is modernizing the technology and capabilities to focus on space environment impacts to SDA, USSF and DoD warfighters. Taking advantage of streamlined research-to-operations (R2O) and cloud architecture features, the SMC, contractor and federally funded research and development center team have developed and are operationalizing flowcharts for a preliminary determination of whether an operational satellite anomaly, an EMI impact or a reported L&PI may have been caused by the space environment. The satellite anomaly flowcharts address single-event effects, event total dose on thinly shielded components, internal charging, and surface charging. The EMI flowcharts address shortwave fades, polar cap absorption, solar radio burst interference, scintillation, auroral clutter/interference, and rain attenuation. The L&PI flowcharts address the same satellite and EMI hazards with the addition of reflected solar illumination or glint, radar ducting/anomalous propagation, meteor shower and sun-in-sensor hazards.

1. SPACE DOMAIN AWARENESS (SDA) ENVIRONMENT TOOLKIT FOR DEFENSE (SET4D)

In April 2020, the Commander, USSPACECOM identified the enhancement of existing and developing of new space domain awareness (SDA) capabilities as his command's number one priority. SDA is reliant on the fusion of space-focused Intelligence, Surveillance, Reconnaissance (ISR) and environmental monitoring. To address this priority, the Space Domain Awareness Environmental Toolkit for Defense (SET4D) is designed to be the United States Space Force (USSF) application suite for all space environment characterization and forecast information. Deployed in cloud-hosted environments, the SET4D goal is to operate on a self-service concept allowing for consumers of information to access customized workspaces for information as needed by the consumer. Data can be tailored to the consumer's mission needs, facilitating a more comprehensive depiction of the environment interaction within the mission envelope. Tailored alerting thresholds allow operators to work without requiring constant monitoring of the environment until necessary.

Serving the broader DOD, IC, and other government entities, SET4D's interface designs will accommodate all user's abilities while ensuring security of data and information through user roles. Access and user role definitions are managed by the Space Flight (2WS/WXZ) at the 557th Weather Wing, who will be able to provide in-tool support for all users. Replicated baselines on all three security enclaves will allow for exploitation of data available and full capability access by consumers in those enclaves.

2. RESEARCH TO OPERATIONS (R2O)

The foundation of SET4D is being built on industry best practices for software and architect engineering for cloud deployment. Ensuring Modular Open Systems Approach (MOSA) within the system to enhance the adaptability to

an ever-changing mission. A key effort to accomplish this goal is architecting to the smallest component. This allows components to be enhanced or replaced without impact to the rest of the system. It also optimizes reuse across the system.

A key benefit to MOSA architecture is the ability to host development sandboxes for academic and industry partners. A Developers Toolkit including operational data feeds and access to common components, such as coordinate transformations, solar wind propagators, and the SET4D visualization tools, will allow partners to develop in an operationally relevant area (technology readiness level of 7). Also available is a guide on industry best practices, and the software development standards used within SET4D. This development follows the Development, Security, and Operations (DevSecOps) Pipeline; a process that facilitates quick promotion of software while ensuring the security requirements are met before exposing the new software to operations.

The end product will be secured, validated, and promoted to a beta exposure to operators for verification in a matter of weeks. This is a dramatic increase from the 15+ months required to integrate black box models into operations. This process also certifies security from day one, and reusability in the system, reducing the sustainment burden to the program.

3. ENERGETIC CHARGED PARTICLE HAZARD ASSESSMENT SYSTEM (ECP-HAS) FLOW CHARTS

As the primary purpose of SET4D is to help users relate the space environment and its impacts on DoD missions, The Aerospace Corporation developed three sets of flow charts to address attribution to the environment. These flow chart capabilities are planned for operationalization in the first few software deliveries of SET4D. In this section, the paper will discuss the first set of flow charts to address satellite anomalies and potential causes from energetic charged particles [21], [22].

3.1 ECP-HAS FC Needs and Overview

The ECP-HAS flow charts are designed to provide a repeatable, rapid satellite anomaly attribution for potential ECP-related, space environment hazards. In the nominal use case, the analyst is provided the time and location of the satellite anomaly, the orbit altitude of perigee and apogee, its inclination, and the orbit type (low Earth orbit (LEO), medium Earth orbit (MEO), geosynchronous/geostationary orbit (GEO), highly elliptical orbit (HEO), etc.). The analyst then collects data from various sources and executes the flowcharts. Due to charged particle motion being constrained by the magnetic field, the analyst will need to covert the orbit Cartesian coordinates (X, Y, Z) into L-shell locations. This magnetic L parameter, which can be computed using the dipole approximation, is defined by:

$$L = \frac{R}{R_E (\cos MLAT)^2} \tag{1}$$

where the MLAT is the geomagnetic latitude of the satellite at the time of the anomaly, R_E is the radius of the Earth, and the R is the square root of the sum of the squares of the Cartesian coordinates.

There are four flowcharts, each addressing a different space environment hazard: surface charging (SC), internal charging (IC), single-event effects (SEE), and event total dose (ETD) on thinly shielded components. The analyst must execute all four flowcharts. Each flow chart results in a conclusion of "H Unlikely" or "Investigate H." In the former case, the preliminary determination is that hazard H is not the cause of the anomaly, and in the latter case, the preliminary determination is that hazard H is possibly the cause and should be investigated further. The entire process from initiation to conclusion is expected to take the analyst 1 to 2 hours.

3.2 Environmental Data for ECP-HAS Flow Charts

In order to execute the ECP-HAS flow charts, the analyst must collect space environment data from a variety of ECP sensors and other key data, e.g. geomagnetic indices and solar wind data. The primary ECP data come from Geostationary Operations Environmental Satellite (GOES), Polar-orbiting Operational Environmental Satellite (POES), and Responsive Environmental Assessment Commercially Hosted (REACH).

3.3   ECP-HAS Hazards

Satellite anomaly attribution is a critical space domain awareness environmental mission. The four space environmental hazards for satellite anomalies are surface charging (SC), internal charging (IC), single-event effects (SEE), and event total dose (ETD) on thinly shielded components, see Fig 1. SC and IC are caused by electrons; and SEE and ETD are caused by protons and heavy ions. Additionally, certain geospace regions, like the inner radiation belt or South Atlantic Anomaly (SAA), slot region, polar cap and outer radiation belt are known locations of potentially high particle fluxes that may cause hazards.

3.3.1   Surface Charging (SC)

The SC sections of the flow chart address two types of SC: auroral and plasma sheet charging. In both cases, electron plasma with energies of keV or higher produces a potential difference on the surface of the spacecraft. If the difference exceeds the breakdown voltage of the spacecraft materials, an electrostatic discharge (ESD) can occur, which can, in turn, cause upsets, phantom commands, and/or damage to the spacecraft. Auroral SC applies only at low altitude, and studies [1] have identified the typical locations when a Defense Meteorological Satellite Program (DMSP) spacecraft is charged to a high voltage relative to the ambient plasma. In order to account for auroral activity, which is typically a requirement for SC, the flow charts have added an activity criterion based on the AE index. Approximately 90 percent of the DMSP charging events occurred for AE>100 nT, even though 100 nT is approximately the median of AE. Plasma sheet charging has been observed on a number of satellites [6] and [16]. The plasma sheet is a region of the magnetosphere that extends from low to high altitudes along magnetic field lines that ultimately intersect the electrical current that flows across the nightside tail of the magnetosphere. To characterize the SC hazard in the plasma sheet, the flow chart logic relies on the patterns of charging observed in an anomaly on the Solar, Anomalous, Magnetospheric Particle Explorer (SAMPEX) Low-Energy Ion Composition Analyzer (LICA) instrument [16].

For both auroral and plasma sheet SC, there are some simplifications necessary to keep the flow charts tractable. Therefore, there remains a small, but finite, probability of SC during quiet times and/or locations outside those indicated in the flow chart. However, the flow chart reflects the conditions and locations for which SC is most often observed.

3.3.2   Internal Charging (IC)

IC occurs when electrons accumulate internal to the spacecraft over hours to days and eventually produce a potential difference large enough to discharge, producing an ESD and the same kinds of consequences as for SC. For the IC hazard, geostationary orbits are considered separately because the GOES >2 MeV electron flux provides an excellent proxy of the hazard for geostationary vehicles at all longitudes. Therefore, the GOES E2MEV threshold value of 3,800 #/cm^2/sr/s corresponds to the 95th percentile. For other orbits, the POES and REACH belt indices are used, with consideration of which regions of space the subject vehicle traverses.

Due to the imperfect correlation between the belt indices and the space environment away from the polar LEO, we have used an 80th percentile threshold for the decisions based on belt indices. This approach is expected to result in the "Investigate IC" conclusion more often than a deeper investigation would conclude that the anomaly was actually caused by IC. We do not have a significant amount of observed electron enhancements for the inner belt/SAA and slot indices from POES and REACH, and the sensors are likely responding in part to protons, so we consider any obvious elevation above steady background level or zero to be a cause for investigation. For POES indices, this means a value greater than zero in the slot indicates an electron enhancement.

3.3.3   Single Event Effects (SEE)

Although the majority of SEE are caused by heavy ions, this flow chart routinely uses the presence of proton radiation as a proxy for both proton and heavy-ion-induced SEE. It is assumed that an SEE threat always exists in the inner belt (L<2 and the SAA), while a transient threat may exist in the slot (L=2-3 and the Extended South Atlantic Anomaly (ESAA) due to a temporary radiation belt or in the outer belt and beyond (L>3) due to a Solar Energetic Particle (SEP) event.

Because of the imperfect correlation between the POES or REACH belt indices and the space environment away from their polar LEO, the flow charts have used an 80th percentile threshold for the decisions based on the belt indices. This approach is expected to result in the "Investigate SEE" conclusion more often than a deeper investigation would conclude that the anomaly was actually caused by SEE.

3.3.4   Event Total Dose (ETD)

The ETD flowchart addresses ETD effects sometimes seen in thinly shielded components, such as solar arrays [15] or other components protected by less than about 20 mils of aluminum (Al) shielding or equivalent. SEPs and transient proton belts are the primary causes of unexpected (i.e., anomalous) event total dose hazards. Transient belts can be formed during SEPs and magnetic storms [14].

For the ETD hazard, geostationary orbits are considered separately because the GOES >5 MeV proton flux provides an excellent proxy of the hazard for geostationary vehicles at all longitudes. Therefore, the GOES P5MEV threshold value of 26 $\#/cm^2/sr/s$ corresponds to the 95th percentile. For other orbits, the POES and REACH belt indices are used, with consideration of which regions of space the subject vehicle traverses. Any vehicle whose orbit traverses the heart of the inner belt (L<1.8) or SAA is considered not susceptible to the ETD hazard because dynamic variations in the trapped and solar populations do not produce significant enhancements over the daily dose provided by the inner belt/SAA.

Due to the imperfect correlation between the belt indices and the space environment away from polar LEO, we have used an 80th percentile threshold for the decisions based on belt indices. This approach is expected to result in the "Investigate ETD" conclusion more often than a deeper investigation would conclude that the anomaly was actually caused by ETD.
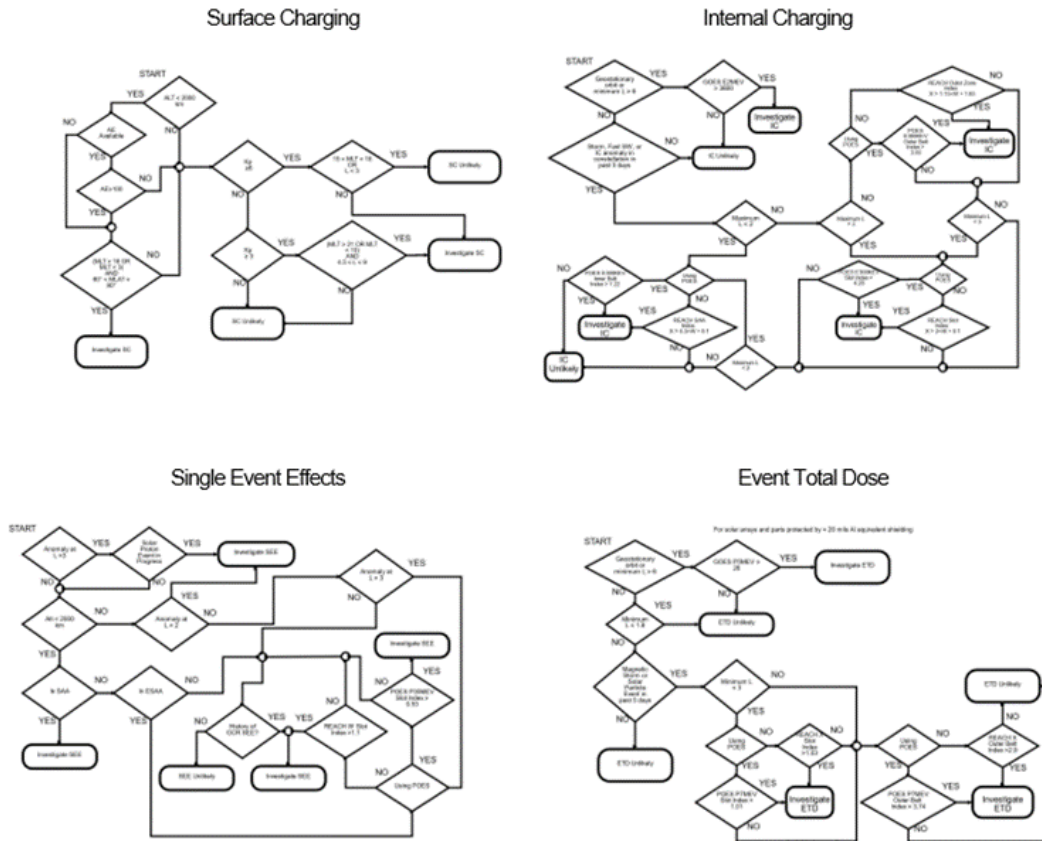
Fig. 1. ECP-HAS Flow Charts for surface charging, internal charging, single event effects, and event total dose

4. SPACE ENVIRONMENT ELCTRO-MAGNETIC INTERFERENCE (SEEMI) FLOW CHARTS

Following on from the previous section and focusing SET4D on helping users relate the space environment and its impacts on DoD missions, The Aerospace Corporation developed a second set of flow charts to address communication, navigation, and command and control link impacts from the environment. In this section, the paper will discuss the flow charts designed to address electro-magnetic interference on links [4].

4.1 SEEMI FC Needs and Overview

The SEEMI flow charts are broken up into two versions depending on the frequency of the EMI event. Two of the hazards only effect HF frequencies, so the flow charts have been separated for HF and above HF frequencies. The SEEMI flow charts are designed to provide a repeatable, rapid EMI attribution for RF signals attributable to environment hazards. In the nominal use case, the analyst is provided the time, location, frequency and RF polarization of the EMI impact, along with information about the RF transmission azimuth and elevation or the satellite used in the trans-ionospheric link. The analyst then collects data from various sources and executes the flow charts. The two flow charts, one for frequencies $\leq$ 30 MHz and one for > 30 MHz include different space environment induced EMI hazards: short-wave fade, polar cap absorption, auroral clutter/interference, equatorial scintillation, solar radio burst radio frequency interference (RFI) rain fade and anomalous propagation (generically called <H>). Working through the appropriate flow chart results in a conclusion of "EMI Unlikely" or "Investigate <H>." In the former case, the preliminary determination is that hazard H is not the cause of the EMI, and in the latter case, the preliminary determination is that hazard H is possibly the cause and should be investigated further. The entire process from initiation to conclusion is expected to take the analyst 1-2 hours.

4.2 Environmental Data for SEEMI Flow Charts

In order to execute the SEEMI flow charts, the analyst must collect space environment and tropospheric weather data from a variety of sources. The primary EMI attribution data come from Geostationary Operations Environmental Satellite (GOES) X-ray and particle sensors, Responsive Environmental Assessment Commercially Hosted (REACH) particle sensors, auroral model output, USSF radio telescopes, scintillation climatology, rain rate and atmospheric profile data.

4.3 SEEMI Hazards

There are seven environmental hazards covered by the SEEMI flow charts. The space environment causes five and the tropospheric weather causes two hazards. The seven hazards are short-wave fade (SWF), polar cap absorption (PCA), auroral clutter/interference, equatorial scintillation, solar radio burst RFI rain fade and anomalous propagation, see Fig 2. The SWF is caused by enhanced X-rays from solar flares. The PCA is caused by enhanced charged particles caused by SEP events. Auroral clutter/interference is caused by plasma density irregularities in intense aurora. Scintillation is caused by electron density irregularities in the equatorial ionosphere. Solar RFI is caused by eruptive events on the Sun. Rain attenuation is caused by absorption of RF signals in rain. Anomalous propagation or ducting is caused by temperature and humidity conditions in the troposphere.

4.3.1 Short-wave Fade

Solar flares produce elevated amounts of electromagnetic radiation, including the X-ray wavelengths which increase the ionization of the ionospheric D layer. High Frequency (HF) communication typically depends on the reflection of signals from the higher F layer of the ionosphere; and therefore, the HF signals must travel through the D layer twice. Increased ionization from a solar flare results in greater absorption of the transmission in the D layer. During large flares the absorption can wipe many if not all HF propagation frequencies on the sunlit side of the Earth. This effect is known as a short-wave fade (SWF). Frequencies above the critical frequency are unaffected by SWF's, so frequencies >30 MHz are unaffected.

Real-time X-ray irradiance is monitored by the GOES Extreme Ultraviolet and X-ray Irradiance Sensors (EXIS) and reports the 1-second X-ray flux in the 0.1-0.8 nm wavelength band. To qualify as a C-class flare, the X-ray flux must fall within the range $10^{-6} \leq F < 10^{-5}$ W/m^2, for M-class $10^{-5} \leq F < 10^{-4}$ W/m^2, and X-class $F \geq 10^{-4}$ W/m^2. The classification of flare by letters (e.g. C, M, X for common, moderate, and extreme), act as multipliers, for example M5.1 equates to a flux of 5.1 x 10^{-5} W/m^2.

The highest affected frequency (HAF) at the sub-solar point with at least 1 dB of fade is

$$f_{HAF,0} = 10\log_{10}\left[\text{flux(W/m}^2)\right] + 65 \text{ MHz} \tag{2}$$

At other geographic locations the HAF becomes lower, based on the solar zenith angle, χ dependence. The degraded frequencies taper off from the maximum as $f_{HAF} = f_{HAF,0} \cos^{0.75} \chi$. For example, an X1.0 flare shows a HAF of 25 MHz at the sub-solar point, decreasing to zero at the day/night terminator. It is necessary to compute the solar zenith angle χ from the location of the D-region ionospheric pierce point (D-IPP).

These absorption calculations determine the amount of fade (dB) at the highest affected frequency at the sub-solar point and can be converted to frequency of interest by using the inverse 1.5 power of the frequency, i.e.

$$A(f) = \left(f_{HAF}/f\right)^{1.5} \text{ dB} \tag{3}$$

with the f_{HAF} being the highest affected frequency after accounting for solar zenith affects. Any absorption greater than 1 dB should be further investigated and will result in the flow chart concluding an "Investigation SWF" result.

4.3.2 Polar Cap Absorption

A polar cap absorption (PCA) event results from the enhanced ionization of the D-layer of the polar ionosphere by high energy protons. A PCA causes a HF radio wave absorption/blackout on polar HF circuits. The impacts can last several days during solar energetic particle events. PCAs are almost always preceded by a significant solar flare with the onset time of the PCA ranging from a few minutes to several hours after the flare.

If the D-IPP is in the polar cap, the daytime and nighttime absorption, A_d and A_n, at the standard frequency $f_{30} = 30$ MHz are calculated depending on the integral proton fluxes J above certain energy E thresholds [23],

$$A_d = 0.115[J(E > 5.2 \text{ MeV})]^{1/2} \text{dB} \tag{4}$$

$$A_n = 0.020[J(E > 2.2 \text{ MeV})]^{1/2} \text{ dB} \tag{5}$$

Day and night are defined by the solar elevation angle $EL_{sun} = 90° - \chi$, with daytime $EL_{sun} > 10°$ and nighttime $EL_{sun} < -10°$, and in the region between day and night, the twilight absorption at 30 MHz, $A(f_{30})$ is obtained as a bilinear composition of the daytime absorption, A_d and nighttime absorption A_n,

In twilight:
$$A(f_{30}) = A_d \left(EL_{sun} + 10°\right)/20° - A_n \left(EL_{sun} - 10°\right)/20° \text{ dB} \tag{6}$$

These absorption calculations determine the amount of fade (dB) at the standard PCA frequency of 30 MHz and can be converted to frequency of interest by using the inverse 1.5 power of the frequency, i.e.

$$A(f) = \left(\frac{f_{30}}{f}\right)^{1.5} A(f_{30}) \text{ dB} \tag{7}$$

Any absorption greater than 1 dB should be further investigated and will result in the flow chart concluding an "Investigation PCA" result.

4.3.3   Auroral Interference

Auroral clutter/interference is caused by back-scatter of RF off the plasma density irregularities in the auroral oval. The RF transmissions will reflect off of the aurora when the transmission path is perpendicular to the magnetic field and the particle precipitation causing the aurora is intense.

Auroral boundary modeling exploits the well-established relationship of equatorward and poleward expansion of the precipitation particles during increased geomagnetic activity [7], [8], [18], [9]. Empirical models of the auroral boundaries have been developed and used in operations for years to help specify the auroral locations in near-real time using only a geomagnetic index, K_p.

Johns Hopkins University Applied Physics Laboratory (JHU/APL) developed an auroral model based on far ultraviolet (FUV) data [28]. Global FUV observations by Thermosphere Ionosphere Mesosphere Energetics and Dynamics (TIMED)/Global Ultraviolet Imager (GUVI) are used to estimate the mean energy (E_o) and energy flux (Q) of precipitating electrons based on an auroral model and airglow Atmospheric Ultraviolet Radiance Integrated Code (AURIC) model [24]. The energy flux for 6 different, increasing geomagnetic activity levels have been calculated. GUVI measures the N_2 Lyman–Birge–Hopfield small (LBHS) 140.0–150.0 nm and Lyman–Birge–Hopfield long (LBHL) 165.0–180.0 nm auroral emissions. The Zhang and Paxton GUVI auroral model is a FUV-based and K_p dependent model of global auroral products (E_o, Q) and was developed using 4 years (2002–2005) of GUVI data. This FUV-based model covers all K_p ranges (0–9). The Zhang and Paxton GUVI auroral model equatorward and poleward latitudinal boundaries have also been determined for each magnetic local time (MLT) and K_p by defining the threshold 1.56e+08 keV/cm2/s (0.25 ergs/cm2/s) and are available for look-up in Cox et al. 2021.

In addition to the empirical aurora models depending on geomagnetic activity indices, there have been successful auroral specifications based off solar wind velocity and magnetic field observations. This solar wind coupling to the hemispheric global power [19] has led to the creation of the Oval Variation, Assessment, Tracking, Intensity, and Online Nowcasting – Prime (OVATION-Prime) model [20]. The OVATION-Prime auroral model is in operations at both NOAA and USSF and provides diffuse, monoenergetic and broadband auroral energy and number fluxes. Each type of aurora (i.e. diffuse, monoenergetic and broadband) is given a separate linear regression fit to the solar wind parameter which best predicts hemispheric global power [19]. This is necessary because each type of aurora responds differently to solar wind driving and because at different latitudes and different local times responses can be quite different.

Auroral clutter/interference is only possible in the auroral zone, so the flow chart's first check is to see if the E-Region ionospheric pierce point (E-IPP) is between the equatorward and poleward boundaries of the aurora.

For HF signals, the threshold for interference was determined by comparing Super Dual Auroral Radar Network (SuperDARN) radar (http://superdarn.jhuapl.edu/) observations at 10 MHz to Defense Meteorological Satellite Program (DMSP) Special Sensor Ultraviolet Spectrographic Imager (SSUSI) observations or auroral energy flux. The radars measure the position and velocity of plasma irregularities in the aurora and SSUSI measure the number and energy flux in the aurora. By combining the observations, it was determined that the threshold for 10 MHz irregularities was 1.248e+08 keV/cm^2/s [27]. The threshold for auroral interference (HF$_{Aur}$) for any HF frequency (f, in MHz) is ascertained by,

$$HF_{Aur} \text{ threshold} = \log_{10}\left(\alpha\left(\frac{f}{f_o}\right)\right) \tag{8}$$

where f_o is 10 MHz and α is 1.248e+8 keV/cm2/s. By scaling the frequency from 3-30 MHz, one gets a range of 7.6 to 8.6 for the $\log_{10}(Q)$ threshold for auroral interference on HF frequencies.

For signals above HF, the flow chart relies on lessons learned from observed auroral clutter at radar facilities [25]. The thresholds used in the operational radar clutter maps is re-used in the flow chart, i.e. $\log_{10}(Q)$ threshold of 9.5 for frequencies > 30 MHz.

For the auroral interference determination, the auroral energy flux at the E-IPP is used. The user will need to check model auroral energy flux output at the EMI location against the appropriate threshold.

4.3.4   Scintillation

Ionospheric scintillation is the rapid fluctuations of radio waves caused by small scale structures in the ionosphere. Severe scintillation conditions can degrade Satellite Communications (SATCOM) and prevent a Global Positioning System (GPS) receiver from locking on to the signal. Less severe scintillation conditions can cause static/noise on SATCOM signals and reduce the accuracy and the confidence of positioning results. Scintillation of radio waves impacts the power and phase of the radio signal. Scintillation is caused by small-scale (tens of meters to tens of km) structure in the ionospheric electron density along the signal path. Equatorial scintillation is confined to regions near the geomagnetic equator, within ±20° [26] and at local times from ~1 hour after sunset to ~1 before sunrise. The analysis uses the F-region IPP to determine if the EMI is within the equatorial region and the F-IPP MLT is between 19-05 LT. Frequencies above 2,400 MHz typically have negligible impacts from scintillation.

The occurrence rate of scintillation is proportional to the F-region electron density which is driven by solar emissions and modulates from high electron densities during solar maximum to lower electron densities during solar minimum. Additionally, there are longitudinal, seasonal, and geomagnetic activity effects that increase and decrease the likelihood of the development of an equatorial plasma bubble (EPB). JHU/APL used the GUVI data to characterize the occurrence rate of the EPBs from 2002-2006 (i.e. solar max-like conditions to solar min-like conditions) [3]. The flow chart uses a minimum EPB rate of 10% to conclude a result of "Investigate Scintillation."

4.3.5 Solar Radio Frequency Interference

Solar RFI is caused by radio frequency noise generated on the sun during large solar flares. Solar radio bursts were discovered during WWII due to impacts on Allied radars and communications. During explosive events on the sun, radio bursts of significant intensity can overwhelm receivers with RFI. Any communication, navigation, or radar system on the sun-lit side of the Earth can be affected, but when the geometry of the receiver is such that the transmitter and sun are in conjunction, the impact can be severe. The conjunction angle, θ, between the azimuth and elevation of the radar/SATCOM antenna and sun is given by,

$$\theta = \cos^{-1}(\sin LAT \sin LAT_{SSP} + \cos LAT \cos LAT_{SSP} \cos(LON - LON_{SSP})) \tag{9}$$

The flowchart considers any conjunction angles ≤ 45° to capture the main lobe and primary side lobes of the antenna and to be hazardous.

The USSF Radio Solar Telescope Network (RSTN) observatories at Sagamore Hill, MA, Keana Point, HI, Learmonth, Australia and San Vito, Italy operate the AN/FRR-95 Radio Interference Measurement Set (RIMS) on eight discrete frequencies using 3 antennas. The solar observatories report significant radio bursts within 2 minutes of occurrence. The Second Weather Squadron (2 WS) issues the WOXX-52 bulletin to warn radio and radar operators of potential solar RFI for an observed radio burst. By choosing the closest frequency and determining the solar conjunction of the receiver, the potential solar RFI impact can be assessed for an EMI event.

4.3.6 Rain Attenuation

Rain fade or attenuation is caused by the absorption of a radio frequency signal by atmospheric rain. The International Telecommunication Union (ITU) Radiocommunication Sector (ITU-R) has determined the specific attenuation due to rain losses, γ_R. ITU-R Recommendations is the name given to set of international technical standards developed by the ITU-R. These Recommendations are the result of studies undertaken by Radiocommunication study groups. ITU-R recommendation P.838 provides experimentally estimated specific attenuation given the frequency, polarization, rain rate and elevation angle [11].

The experimental data for specific attenuation in units of dB/km caused by liquid precipitation takes on a Power law relationship,

$$\gamma_R = kR^{\alpha} \tag{10}$$

with rain rate, R, given in mm/hr. The Power Law parameters are,

$$k = [k_H + k_V + (k_H - k_V)\cos^2 EL \cos 2\tau]/2 \tag{11}$$

$$\alpha = [k_H\alpha_H + k_V\alpha_V + (k_H\alpha_H - k_V\alpha_V)\cos^2 EL \cos 2\tau]/2k \tag{12}$$

where EL is the elevation angle and τ is the polarization tilt angle relative to the horizontal (τ = 45° for circular polarization). If the analyst does not know the polarization, assume circular polarization. The horizontal and vertical polarized coefficients, k_H and α_H, and k_V and α_V, respectively, for a given frequency are listed in [11].

The absolute rain fade (dB) can be determined if the rain cell volume along the RF link path is known. See [2], the average horizontal rain cell sizes were determined by analyzing three years (i.e. 240,000) of rain cells and determined to fit the simple relationship of 3.3R-0.08 and range from 3.1-2.3 km for light rain to tropical rain. The vertical extent/thickness of rain varies from <1 km to 5 km thickness as rain rate increases from 2.5-100 mm/hr. Consequently, using specific attenuation of 1 dB/km would lead to typical fades of ~3 dB (50% loss) for low elevation RF links in downpours and tropical rain for isolated cells and more attenuation for widespread convection with numerous cells along the RF link.

In order to calculate the absolution attenuation, multiply the specific attenuation by an estimate of the path length through the rain. The simple assumption that the RF link's path through the rain is from the ground site to the freezing level, above which the water is frozen and not causing the attenuation from equation 10. The path length to the freezing level, $PL_{0°}$, will be defined by the elevation angle and the freezing level height above the ground, $AGL_{0°}$.

$$PL_{0°} = \frac{AGL_{0°}}{\sin EL} \tag{13}$$

In the event the user is unable to access model data for freezing level heights, National Centers for Environmental Prediction (NCEP) reanalysis and comparison to Tropical Rainfall Measuring Mission (TRMM) satellite data can be used to estimate the freezing level heights for tropical, mid-latitudes and polar latitudes [10].

4.3.7   Anomalous Propagation and Ducting

Anomalous propagation or ducting of radar signals is caused by temperature and humidity conditions in the atmosphere. The International Telecommunication Union (ITU) Radiocommunication Sector (ITU-R) has determined the refraction of radiowaves is controlled by the refractivity index, N [12]. By assessing the vertical refractivity gradient ($\Delta N/km$) of the atmosphere above the ground site, the user can determine the propagation characteristics of Very High Frequency (VHF) and Ultra High Frequency (UHF) radiowaves.

The refractivity index, N, is defined by

$$N = \frac{77.6}{T}\left(P + 4810\frac{e}{T}\right) \tag{14}$$

where T is the temperature (K), P is the total atmospheric pressure (hPa) and e is the water vapor pressure (hPa). The water vapor pressure is calculated using the saturation vapor pressure (e_s) and relative humidity (H),

$$e = \frac{H \cdot e_s}{100} \tag{15}$$

and the saturation vapor pressure (e_s) is defined by,

$$e_s = EF_{water} \cdot 6.1121 \cdot exp\left[\frac{\left(18.678 - \frac{T}{284.5}\right) \cdot T}{T + 257.14}\right] \tag{16}$$

where T is the temperature (°C), valid from -40° to +50°C. The specific emission factor (EF) of water is defined as,

$$EF_{water} = 1 - 10^{-4}[7.2 + P \cdot (0.0320 + 5.9 \cdot 10^{-6} \cdot T^2)] \tag{17}$$

where P is the total atmospheric pressure (hPa) and T is the temperature (°C). Finally, using the vapor pressure, temperatures, and isobaric pressures in Eq. (14) yields the refractivity index in "N units." The refractive index must be computed at each height and then the refractivity gradient can be computed between adjacent heights. By assessing the vertical refractivity gradient ($\Delta N/km$), one can determine the atmospheric propagation characteristics, if the vertical refractivity gradient is <-157 then ducting is likely.
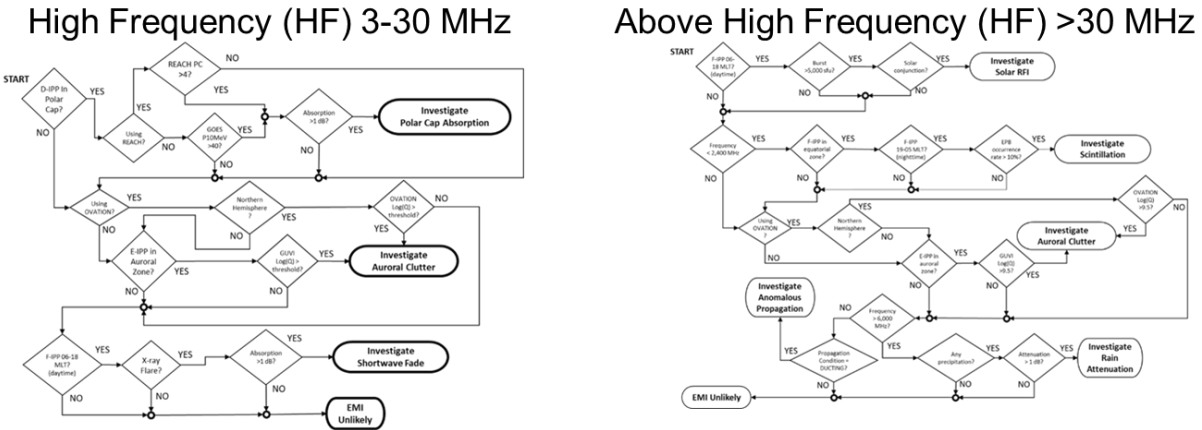
Fig. 2. SEEMI Flow Charts for EMI hazards for HF (3-30 MHz) and above HF (>30 MHz) links

5. LAUNCH AND PREDICTED IMPACTS (L&PI) FLOW CHARTS

Finally, a third set of flow charts to help users relate the space environment and its impacts on DoD missions was developed by The Aerospace Corporation to address impacts from the environment on the missile warning mission. In this section, the paper will discuss the flow charts designed to address L&PI environmental impacts [5].

5.1 L&PI FC Needs and Overview

In support of the missile warning mission, the L&PI flow charts have been designed in three versions depending on the source of the L&PI report. The L&PI flow charts are designed to provide a repeatable, rapid attribution for L&PI events attributable to environment hazards. In the nominal use case, the analyst is provided the time, location of L&PI, and source of the report (i.e. radar site or satellite). The analyst then collects data from various sources and executes the flow charts. The flow charts address ground-based hazards including solar radio burst interference, auroral clutter, anomalous propagation, and meteor showers, while the space-based hazards include single event effects, surface and internal charging, sun-in-sensor, solar illumination glint and meteor showers, see Fig 3. Working through the appropriate flow chart results in a conclusion of "L&PI Unlikely" or "Investigate <H>." In the former case, the preliminary determination is that hazard H is not the cause of the L&PI, and in the latter case, the preliminary determination is that hazard H is possibly the cause and should be investigated further. The entire process from initiation to conclusion is expected to take the analyst 1-2 hours.

5.2 Environmental Data for L&PI Flow Charts

In order to execute the L&PI flow charts, the analyst must collect space environment and tropospheric weather data from a variety of sources. The ECP data come from Geostationary Operations Environmental Satellite (GOES), Polar-orbiting Operational Environmental Satellite (POES), and Responsive Environmental Assessment Commercially Hosted (REACH). Additionally, the analyst must collect space environment and weather data from auroral model output, geomagnetic indices, solar wind data, USSF radio telescopes, scintillation climatology, meteor shower intensities, rain rate and atmospheric profile data.

5.3 L&PI Hazards

There are three separate flow charts for L&PI with multiple hazards on each. The three flow charts are based off which platform reported the L&PI, i.e. a ground-based radar, a HEO satellite, or a GEO satellite.

5.3.1   Surface Charging

The L&PI surface charging hazard is the same as the ECP-HAS surface charging hazard. See §3.3.1.

5.3.2   Internal Charging

The L&PI internal charging hazard is the same as the ECP-HAS internal charging hazard. See §3.3.2.

5.3.3   Single Event Effects

The L&PI single event effects hazard is the same as the ECP-HAS single event effects hazard. See §3.3.3.

5.3.4   Auroral Interference and Clutter

The L&PI auroral clutter hazard is the same as the SEEMI auroral clutter hazard. See §4.3.3.

5.3.5   Solar Radio Frequency Interference

The L&PI solar RFI hazard is the same as the SEEMI solar RFI hazard. See §4.3.5.

5.3.6   Anomalous Propagation and Ducting

The L&PI anomalous propagation hazard is the same as the SEEMI anomalous propagation hazard. See §4.3.7.

5.3.7   Meteor Shower Interference

The L&PI flow charts need to assess the likelihood that a meteor streak or fireball could have produced a false L&PI event from either ground-based radars or space-based missile warning satellites. Meteors are pieces of dust and debris from space that burn up in Earth's atmosphere, where they can create bright streaks across the night sky that can be misinterpreted as missiles or satellites. The meteor shower flux is forecasted annually by NASA's Meteoroid Environment Office using the standard double-exponential shape of a meteor shower activity profile. Meteor shower models [17] are based off the population index and include an approximate sporadic background [13]. The sporadic background is much less well understood and parameterized than the showers but can add an appreciable amount to the shower meteor rates. The Zenith Hourly Rate (ZHR) describes the rate at which a meteor shower produces visible meteors at magnitude +6.5 brightness. After reviewing the meteor shower flux forecast for 2016 through 2025, it was determined that the 80th percentile value for Zenith Hourly Rate (ZHR) when combining the sporadic and storm fluxes is 27.

5.3.8   Sun-in-Sensor

During days near equinox, GEO satellite optical sensors near midnight local time can have solar illumination intrusion into optical sensors, this is called the Sun-in-Sensor hazard. In order to calculate the hazard, the analyst will use the LAT/LON of the satellite and anti-sub-solar point (assp). The anti-sub-solar point is the conjugate of the sub-solar point and is at midnight.

$$\varphi = \cos^{-1}\left[\sin LAT_{sat} \sin LAT_{assp} + \cos LAT_{sat} \cos LAT_{assp} \cos\left(LON_{sat} - LON_{assp}\right)\right] \quad (18)$$

when the central angle difference between the assp and the sub-satellite point (satellite's LAT/LON) is ≤ 15° then sun-in-sensor hazard is likely. This equates to approximately within 37 days of equinox and within 60 minutes of midnight, depending on how far from equinox.

5.3.9   Solar Illumination Glint

For solar illumination glint to be a L&PI hazard, two conditions must be met; the L&PI location must be a location of high surface albedo (e.g. water, snow, or ice) and the geometry of the sun, L&PI location and satellite must be aligned so that the relative glint angle is small. The relative glint angle is defined by the elevation and azimuth of the sun and satellite. For the relative glint angle to be small, the elevations of the sun and satellite must be approximately equal, and the azimuth of the sun and satellite differ by approximately 180°.

To determine the relative glint angle, ϕ,

$$\phi = \cos^{-1}\left[(\cos\chi \cos\theta) + \left(\sin\chi \sin\theta\cos\left(\pi - (AZ_{sat} - AZ_{sun})\right)\right)\right] \tag{19}$$

where χ is the solar zenith angle, θ is the zenith angle of the satellite (i.e. complementary to the satellite's elevation angle) and AZ_{sat} and AZ_{sun} are the azimuth of the satellite and sun from the L&PI location with respect to North, respectively. If the relative glint angle, ϕ is > 0 and ≤ 36°, then glint is possible depending on the surface reflectivity.

The determination of high albedo is controlled by the surface condition types of water, snow, or sea ice of any concentration. In other words, dry land has a low albedo and will not cause glint, while snow covered land, water, ocean with any amount of ice concentration can cause glint.

Both the small relative glint angle and high albedo must be present for the glint hazard to be a potential cause of a L&PI.
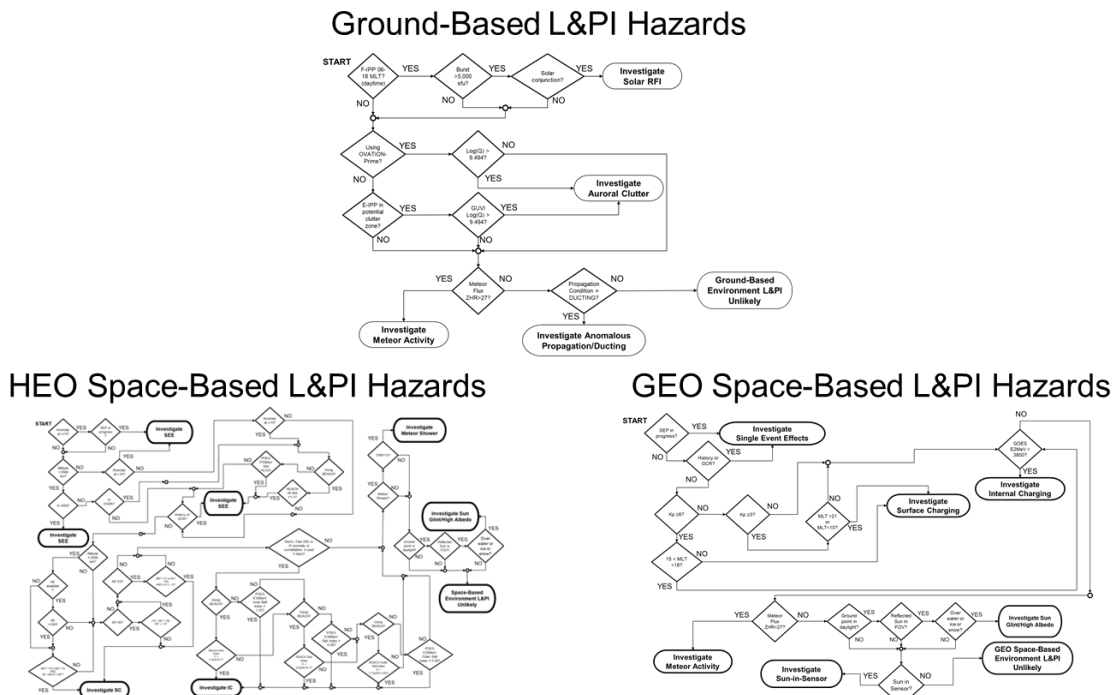

Fig. 3. L&PI Flow Charts for ground-based and space-based environmental hazards

6. SUMMARY

To address the critical need for environmental attribution of impacts on satellite, communication and missile warning operations, The Aerospace Corporation developed three sets of flow charts for integration into the SET4D cloud architecture. These three flow charts use environmental observations and model output along with algorithms, date/time, and location information to characterize the hazards for satellite anomalies from charged particles, link interference and missile warning impacts. The paper describes the SET4D architecture, research to operations process and the three different flow charts. By leveraging the streamlined R2O process designed in the SET4D cloud architecture, these space environment capabilities will be brought on-line into operations much quicker than ever before.

7. REFERENCES

[1] Anderson, P. C. (2001), "A survey of spacecraft charging events on the DMSP satellite in LEO," Proceedings of the 7th International Spacecraft Charging Technology Conference, Noordwijk, The Netherlands, April 23–27, 2001.

[2] Crane, Robert K. (1982), A two component rain model for the prediction of attenuation statistics, Radio Sci., 1982, 17, 1371-1387.

[3] Comberiate, J., and L. J. Paxton (2010), Global Ultraviolet Imager equatorial plasma bubble imaging and climatology, 2002–2007, J. Geophys. Res., 115, A04305, doi:10.1029/2009JA014707.

[4] Cox, J.M., T.P. O'Brien, A. J. Boyd and D. G. Brinkman (2021), A human-in-the-loop decision tool for preliminary assessment of the relevance of the space environment to electro-magnetic interference, Aerospace Report Number TOR-2021-00972, The Aerospace Corporation, El Segundo, CA, Mar 12, 2021.

[5] Cox, J.M., T.P. O'Brien, A. J. Boyd and L.J. Gelinas (2021), A human-in-the-loop decision tool for preliminary assessment of the relevance of the space environment and weather conditions to Launch and Predicted Impacts, Aerospace Report Number TOR-2021-01499, The Aerospace Corporation, El Segundo, CA, June 25, 2021.

[6] Fennell, J. F., and J. L. Roeder (2007), HEO satellite surface and frame charging and SCATHA low-level frame charging, Aerospace Report Number TR-2007(8570)-1, The Aerospace Corporation, El Segundo, CA, November 15, 2007.

[7] Gussenhoven, M. S., D. A. Hardy, and N. Heinemann, (1983), Systematics of the Equatorward Diffuse Auroral Boundary, J. Geophys. Res., 88, pp. 5692-5708.

[8] Hardy, D. A., M. S. Gussenhoven, and E. Holeman (1985), A Statistical Model of Auroral Electron Precipitation, J. Geophys. Res., 90, 4229-4248.

[9] Hardy, D. A., E. G. Holeman, W. J. Burke, L. C. Gentile, and K. H. Bounar, (2008), Probability distributions of electron precipitation at high magnetic latitudes, J. Geophys. Res., 113, A06305, doi:10.1029/2007JA012746.

[10] Harris, G. N., K. P. Bowman and D-B Shin, (2000), Comparison of freezing-level altitudes from the NCEP reanalysis with TRMM precipitation radar Brightband data, J. Clim., 13, 4137–4148.

[11] ITU-R P.838-3 (2005), Specific attenuation model for rain for use in prediction methods.

[12] ITU-R P.453.14 (2019), The radio refractive index: its formula and refractivity data.

[13] Jenniskens, P. (1994), Meteor stream activity, I. The annual streams, Astronomy and Astrophysics, 287, 990-1013 (1994).

[14] Lorentzen, K. R.; J. E. Mazur; M. D. Looper; J. F. Fennell; and J. B. Blake (2002), "Multisatellite observations of MeV ion injections during storms," J. Geophys. Res., 107(A9), 1231, doi:10.1029/2001JA000276, 2002.

[15] Marvin, D. C., and D. J. Gorney (1991), "Solar proton events of 1989: Effects on spacecraft solar arrays," J. Spacecraft, 28(6), 713-9, 1991.

[16] Mazur, J. E. et al. (2010), "The timescale of surface charging events," Proceedings of the 11th International Spacecraft Charging and Technology Conference, Albuquerque, NM, September 20–24, 2010.

[17] Moorhead, A. V., et al., (2019), Meteor shower forecasting in the near-Earth space, Journal of Spacecraft and Rockets, doi:10.2514/1.A34416.

[18] Newell, P. T., T. Sotirelis, J. M. Ruohoniemi, J. F. Carbary, K. Liou, J. P. Skura, C.-I. Meng, C. Deehr, D. Wilkinson, and F. J. Rich (2002), OVATION: Oval variation, assessment, tracking, intensity, and online nowcasting, Annales Geophysicae 20: 1039–1047.

[19] Newell, P. T., T. Sotirelis, K. Liou, C.-I. Meng, and F. J. Rich (2007), A nearly universal solar wind-magnetosphere coupling function inferred from 10 magnetospheric state variables, J. Geophys. Res., 112, A01206, doi:10.1029/2006JA012015.

[20] Newell, P. T., T. Sotirelis, and S. Wing (2009), Diffuse, monoenergetic, and broadband aurora: The global precipitation budget, J. Geophys. Res., 114, A09207, doi:10.1029/2009JA014326.

[21] O'Brien, T.P. et al. (2012), A human-in-the-loop decision tool for preliminary assessment of the relevance of the space environment to a satellite anomaly, Aerospace Report TOR-2011(8181)2A, May 10, 2012.

[22] O'Brien, T. P. et al. (2020), A human-in-the-loop decision tool for preliminary assessment of the relevance of the space environment to a satellite anomaly—Update with REACH and MEO, Aerospace Report Number TOR-2020-00349, The Aerospace Corporation, El Segundo, CA, Jan 31, 2020.

[23] Sauer, H. H., and D. C. Wilkinson (2008), Global mapping of ionospheric HF/VHF radio wave absorption due to solar energetic protons, Space Weather, 6, S12002, doi:10.1029/2008SW000399.

[24] Strickland, D.J., Bishop, J., Evans, J.S., Majeed, T., Shen, P.M., Cox, R.J., Link, R., Huffman, R.E., (1999), Atmospheric ultraviolet radiance integrated code (AURIC): theory, software architecture, inputs, and selected results. Journal of Quantitative Spectroscopy & Radiative Transfer 62, 689.

[25] Tsunoda, R. T. (1991), Auroral-Clutter Predictions for Flyingdales, England, PL-TR-911-2198.

[26] Whalen, J.A. (1997), Equatorial bubbles observed at the north and south anomaly crests: Dependence on season, local time, and dip latitude, Radio Science, Vol 32, Number 4, Pages 1559-1566, July-August 1997.

[27] Zhang, Y., E.J. Mitchell, E.S. Miller, J. Comberiate, R.K. Schaefer and L. Paxton (2018), Personal Conversation with JHU/APL, Sep 7, 2018.

[28] Zhang, Y., and L. Paxton (2008), An empirical Kp-dependent global auroral model based on TIMED/GUVI FUV data, JASTP 70 (2008) 1231–1242.